ACS APPLIED MATERIALS & INTERFACES

www.acsami.org

Research Article

Composite Graded Melt Electrowritten Scaffolds for Regeneration of the Periodontal Ligament-to-Bone Interface

Nasim Golafshan, Miguel Castilho, Arwa Daghrery, Morteza Alehosseini, Tom van de Kemp, Konstantinos Krikonis, Mylene de Ruijter, Renan Dal-Fabbro, Alireza Dolatshahi-Pirouz, Sarit B. Bhaduri, Marco C. Bottino,* and Jos Malda*

Cite This: *ACS Appl. Mater. Interfaces* 2023, 15, 12735−12749

Read Online

ACCESS | Metrics & More | Article Recommendations | Supporting Information

ABSTRACT: Periodontitis is a ubiquitous chronic inflammatory, bacteria-triggered oral disease affecting the adult population. If left untreated, periodontitis can lead to severe tissue destruction, eventually resulting in tooth loss. Despite previous efforts in clinically managing the disease, therapeutic strategies are still lacking. Herein, melt electrowriting (MEW) is utilized to develop a compositionally and structurally tailored graded scaffold for regeneration of the periodontal ligament-to-bone interface. The composite scaffolds, consisting of fibers of polycaprolactone (PCL) and fibers of PCL-containing magnesium phosphate (MgP) were fabricated using MEW. To maximize the bond between bone (MgP) and ligament (PCL) regions, we evaluated two different fiber architectures in the interface area. These were a crosshatch pattern at a 0/90° angle and a random pattern. MgP fibrous scaffolds were able to promote *in vitro* bone formation even in culture media devoid of osteogenic supplements. Mechanical properties after MgP incorporation resulted in an increase of the elastic modulus and yield stress of the scaffolds, and fiber orientation in the interfacial zone affected the interfacial toughness. Composite graded MEW scaffolds enhanced bone fill when they were implanted in an *in vivo* periodontal fenestration defect model in rats. The presence of an interfacial zone allows coordinated regeneration of multitissues, as indicated by higher expression of bone, ligament, and cementoblastic markers compared to empty defects. Collectively, MEW-fabricated scaffolds having compositionally and structurally tailored zones exhibit a good mimicry of the periodontal complex, with excellent regenerative capacity and great potential as a defect-specific treatment strategy.

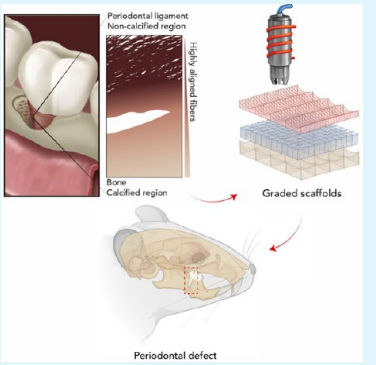

KEYWORDS: *periodontitis, melt electrowriting, bone regeneration, periodontal ligament, interface*

1. INTRODUCTION

The interfaces between bone and connective tissues, e.g., cartilage, ligament, and tendon, are characterized by spatial changes in cell phenotype and matrix composition and organization.[1] These changes result in graded biomechanical properties that allow the transmission of a load without creating stress concentrations.[2] In some interface regions, such as the bone−cartilage or bone−ligament interfaces, differences in mechanical properties (e.g., stiffness), can reach 3−4 orders of magnitude within a very short distance.[3] Undoubtedly, this highlights the clinical challenge of regenerating these structurally and functionally complex tissue interfaces.[4] One of the interfaces that is particularly difficult to regenerate is the periodontal ligament-to-bone (PDL−bone) interface. The PDL is situated between the roots of the teeth and the alveolar bone sockets.[5] Collagen fibers, known as Sharpey's fibers, form a firm connection between the tooth cementum and alveolar bone. These fibers are partially mineralized and inserted in the alveolar bone/cementum at an oblique angle, which ensures transmission of the occlusal force from the tooth to the alveolar bone.[5]

In the event of periodontitis, a widespread chronic inflammatory disease, the PDL−bone interface gets impaired, leading to tooth mobility, which without proper treatment can ultimately result in tooth loss.[6] In Europe alone, periodontitis affects approximately 40% of older people.[7] This results in significant loss of quality of life and increased healthcare costs.[8] Conventional treatment methods, including but not limited to scaling and root planing, often result in disorganized tissue formation with inferior properties compared to their native counterpart.[9−11] This ultimately leads to poor long-term outcomes and high failure rates, extenuating the need for the development of therapeutic strategies for regeneration of the PDL−bone interface.[12,13]

Received: November 25, 2022
Accepted: February 15, 2023
Published: February 28, 2023

https://doi.org/10.1021/acsami.2c21256
ACS Appl. Mater. Interfaces 2023, 15, 12735−12749

Current regenerative efforts are typically directed toward the development of composite,[14,15] stratified scaffolds,[16] with graded structures and physicochemical compositions. There are many conventional techniques to produce 3D structures with characteristics to enhance tissue regeneration. Additive manufacturing (AM) allows for the fabrication of defect- and tissue-specific scaffolds with the ability to mimic native tissue morphology and biomechanics through various 3D-printing technologies. A number of these techniques have been successfully used to engineer multilayered fiber support structures to capture some of the complexity of native tissues, such as the interface between bone and ligaments; however, none of them could fully replicate the structural organization and long-term functional properties of native interface tissues. More recently, melt electrowriting techniques have been introduced as a 3D-printing technology to obtain organized microfiber scaffolds. This 3D-printing technology is distinct from others in that the high fiber resolution (2−20 μm) is accompanied by the ability to 3D print structures with controlled microgeometries. This differs from other 3D-printing technologies that have resolution limits of around 20 μm or are challenged in fabricating controlled microgeometries. In fact, this ability to create defined scaffold microgeometries is the reason electrowriting gives fiber scaffolds significant advantages in the regeneration of native tissue interfaces.[17]

Early attempts, including scaffolds with PDL- and bone-specific regions using polymer fibers,[4] have shown encouraging results. Notably, bilayered scaffolds with aligned fibers for the PDL zone[4] and graded polycaprolactone (PCL) scaffolds with distinct fiber alignments for bone and ligament zones[18] have led to positive prospects in the quest to regenerate the periodontal ligament-to-bone interface. One of the particularly difficult interfaces to regenerate is the periodontal ligament-to-bone (PDL−bone) interface. Previous research has used MEW to create scaffolds tailored to bone and PDL regions.[18,19] However, these studies did not produce a graded scaffold that mimics the native periodontal complex mechanical function. In this study, we not only focused on creating zonal-specific scaffolds for bone and PDL but also investigated the use of an interfacial zone to enhance the bond between the bone (MgP) and ligament (PCL) regions, with the goal of improving the overall mechanical performance and tissue-specific regenerative outcome. For instance, tissue-specific bilayered PCL scaffolds were fabricated by melt electrowriting (MEW). The resulting scaffolds encompassing two distinct zones, with specific fiber architecture and composition, were able to promote differentiation of human-derived periodontal ligament stem cells (hPDLSCs) toward ligament and bone lineage dependent on the fiber configuration and composition.[19,20]

Therefore, the control of fiber configuration and composition is necessary for the PDL−bone interface regeneration. However, existing scaffolds lack the appropriate fiber configuration and composition to enable the regeneration of such complex interfaces. The fiber organization can promote ligamentogenesis and drive PDL-like tissue formation,[20] while the chemical composition with osteoconductive properties can promote bone regeneration. Among the osteoconductive materials, magnesium phosphate (MgP) bioceramics have shown great ability to promote bone and degrade *in vivo*.[21,22] Thus, we hypothesize that an osteoconductive scaffold with a graded blend of MgP bioceramics and polycaprolactone (PCL) with a tissue-specific, stable interfacial zone and structural properties can facilitate long-term bone-to-ligament interface regeneration. Furthermore, the one-step fabrication strategy to develop compositionally and structurally tailored graded scaffolds using MEW can achieve this challenging requirement. The effect of MgP content on the MEW processing was investigated in order to obtain reproducible and mechanically stable fibrous scaffolds with micrometer sizes and osteoconductive ability. The scaffold mechanical stability was investigated under uniaxial tensile loading, while osteogenic properties were addressed *in vitro* over 21 days in both expansion and osteogenic media. Further, the interfacial adhesion properties of graded scaffolds were evaluated *ex vivo*. Finally, the ability of as-fabricated graded scaffolds to promote synchronized regeneration of bone and PDL ligament was determined in an *in vivo* orthotopic periodontal rat model over 6 weeks.

2. EXPERIMENTAL SECTION

2.1. Biomaterial MgP-Based Bioceramic Ink Preparation. MgP-based inks were prepared by incorporating commercial magnesium phosphate ($Mg_3(PO_4)_2$ (Sigma-Aldrich, Germany) at 10 and 20 wt % concentration into PCL (PURASORB PC 12, Corbion Inc., Netherlands), here abbreviated as 10MgP and 20MgP, respectively. Incorporation of MgP was performed by first dissolving PCL in dichloromethane (DCM, Honeywell, USA) for 6 h with the subsequent addition of MgP under constant stirring. Blend homogenization was obtained by overnight stirring. Finally, the MgP-based ink was precipitated into pure ethanol (Sigma-Aldrich, Germany), and the precipitate was dried in air at room temperature overnight.

2.2. Particle Size and Thermogravimetric Analyses. The MgP particle morphology and size were analyzed using scanning electron microscopy (SEM, FEI Quanta 200 ESEM FEG, USA). Prior to the imaging, MgP particles were sputter-coated with gold for a thickness of 6 nm (Q150T S/E/ES, UK). SEM images were then analyzed to quantify MgP particle distribution with the help of ImageJ software (Version 7.0, National Institutes of Health, USA). Differential scanning calorimetry was performed (DSC Q200, TA Instruments, USA). In brief, PCL pellets, MgP particles, and 20MgP pellets were placed in T zero aluminum pans (Mettler-Toledo AG, Greifensee, Switzerland) and sealed. The measurements were performed between 25 and 300 °C with a ramp rate of 10 °C/min, under a nitrogen flow of 50 mL/min. The heat flow change was measured as a function of temperature with reference to an empty pan.[23]

2.3. Melt Electrowriting of MgP-Based Bioceramic Ink. Prior to melt electrowriting, MgP-based inks of different compositions (10 and 20 wt % MgP) were thermally treated at 140 °C for 6 h. Next, inks were transferred to a 5 mL metallic cartridge. The ink processing compatibility was systematically evaluated according to key MEW parameters, namely the applied voltage (6−9 kV), collection speed (5−40 mm/sec), temperature (100 °C), and pressure (80 kPa), to evaluate the stable jet formation (Figure S1), fiber diameter, and morphology. The temperature and pressure were chosen based on the properties of the raw materials and kept constant during the experiment.

Fibrous scaffolds (20 mm × 20 mm, n = 3) with varying square-shaped fiber strand spacings (500, 750, and 1000 μm) and numbers of stacked layers (1, 5, and 10) were fabricated for each composition at a melting temperature of 100 °C, a pressure of 80 kPa, and a voltage between 6 and 9 kV. All scaffolds were prepared with a 23G nozzle using a 3DDiscovery Evolution MEW machine (RegenHU, Switzerland). All scaffolds were designed using BioCAD software (RegenHU).

2.4. Printed MgP-Based Scaffold Accuracy. Fiber morphology and diameter were evaluated by SEM. In addition, scaffolds were imaged with an upright microscope (Olympus BX43, Japan), and acquired images were processed with ImageJ software. Printing

https://doi.org/10.1021/acsami.2c21256
ACS Appl. Mater. Interfaces 2023, 15, 12735−12749

accuracy was quantified using a quality number, $Q_{alignment}$, determined as

$$Q_{alignment} = \frac{A_{measured}}{A_{expected}} \leq 1 \quad (1)$$

where $A_{measured}$ and $A_{expected}$ indicate the experimental and theoretical areas, respectively. $A_{expected}$ was estimated as

$$A_{expected} = n_{squares} \times (\text{fiber spacing} - \Phi_{\text{fiber diameter}})^2 \quad (2)$$

At least three samples from each composition were measured.

2.5. Melt Electrowriting of Graded Scaffolds. MEW graded scaffolds were fabricated using a 3D Discovery Evolution MEW machine (RegenHU, Switzerland). The crosshatch 0/90 architecture with 500 μm fiber spacing was designed for the bone zone using 20MgP, and an aligned fiber architecture was designed for the PDL zone using PCL.

The proposed graded scaffolds were designed to have three distinct zones composed of a bone zone (20MgP, fiber spacing 500 μm), an interfacial zone, and a PDL zone (highly aligned PCL fibers, fiber spacing 50 μm). The bone zone represented 70% of the total height of the scaffold, while the interfacial and PDL zones represented 10% and 20% of the total height, respectively.

Two distinct architectures were designed for the interfacial zone.

(1) A graded scaffold was composed of a square crosshatch architecture, henceforth referred to as 20MgP-crsht, with intersecting sets of parallel lines with a strand spacing of 250 μm.[19]
(2) A graded scaffold was composed of randomly oriented fibers, henceforth referred to as 20MgP-rnd.

The 20MgP composite formulation and pure PCL were loaded into cartridges with 23G and 27G nozzles, respectively. Prior to printing, the metallic cartridges were heated to 100 and 80 °C for 20MgP and PCL, for 45 min, and subsequently dispensed at 0.08 and 0.1 MPa system pressures, respectively. A summary of the printing conditions is provided in Table 1.

Table 1. MEW Parameters for Printing the Graded Scaffolds

zone	collection speed (mm/s)	collection distance (mm)	applied voltage (kV)
20MgP/bone zone	5	3.5	7
PDL/ligament zone	40	4	6
rnd/interfacial zone	5	4	6.8
crsht/interfacial zone	13	4	6.8

2.6. Physical and Chemical Properties. The chemical structure of the developed scaffolds was analyzed via Fourier transform infrared (FTIR) spectroscopy using an attenuated total reflectance spectrometer (PerkinElmer Spectrum 100, USA). FTIR spectra were obtained with a 4 cm^{-1} resolution within the 400−3500 cm^{-1} range. Scanning electron microscopy was performed to evaluate the morphology of the scaffolds as mentioned above. Energy dispersive X-ray spectroscopy (EDS, USA) analysis was conducted to assess the inorganic phase after the printing of the scaffolds. Prior to the imaging, the scaffolds were coated with ab 8 nm gold layer. Based on the SEM images, the fiber diameter, porosity, and fiber spacing of printed scaffolds (20MgP-crsht, 20MgP-rnd, 20MgP, crsht, rnd, and PDL) were measured by using ImageJ, ver. 7.

2.7. Ion Release. Melt electrowritten 20MgP scaffolds (20 mm × 20 mm length) with 500 μm fiber spacing were immersed in 0.1 M Tris-HCl (tris(hydroxymethyl)aminomethane, Sigma-Aldrich, Germany) at 37 °C. The cumulative ion release profile of magnesium and phosphorus ions was recorded utilizing inductively coupled plasma mass spectrometry (ICP-MS, Varian, Darmstadt, Germany) at different incubation periods (1, 3, 5, 10, and 21 days). To quantify the concentration of released ions, the solutions were diluted 10× in 1.3 v/v% HNO_3 (65% Suprapur, Merck, Schwalbach, Germany) and measured against standard solutions of magnesium and phosphorus (Merck, Schwalbach, Germany).

2.8. Mechanical Properties. The tensile mechanical properties of PCL, 10MgP, and 20MgP were evaluated under uniaxial tensile loading using a dynamic mechanical analyzer (DMAQ800, TA Instruments, USA) equipped with a 50 N load cell. 20MgP-na referred to the samples without an interfacial zone, used as control. Rectangular samples (1 cm width × 30 mm length × 1 mm thickness) were loaded at a deformation rate of 2 mm/min at room temperature until failure. The tensile modulus, tensile yield strain, and tensile toughness were determined from engineered stress−strain curves. The tensile modulus was determined using a least-squares fit of the initial slope of the stress−strain elastic region (0.1−0.5 mm/mm), the tensile yield point was defined as the point where nonlinear deformation begins, and the tensile toughness was obtained as the area under the stress−strain curve until the yield point. Subsequently, to determine the interfacial mechanical properties between bone (20MgP composition, crosshatch structure, 500 μm fiber spacing) and PDL regions (PCL, highly aligned fibers, 50 μm fiber spacing) of the graded scaffolds with two interface architectures (crsht and rnd), a delamination test was performed. Rectangular samples (10 mm width × 20 mm length × 1 mm thickness) with an interface contact area of 200 mm^2 were mounted on a dynamic mechanical tester loaded at a rate of 2 mm/min, and the interfacial modulus, interfacial yield strain, and interfacial toughness were obtained as previously described above.

2.9. *In Vitro* Cell Culture. To confirm the *in vitro* cell compatibility and osteogenic potential of the developed MgP-based MEW scaffolds, cylindrical samples (5 mm diameter × 1 mm height) of PCL, 10MgP, and 20MgP were cultured *in vitro* with bone marrow derived human mesenchymal stem cells (hMSCs, harvested according to the protocol described elsewhere,[24] passage 4) for 21 days in α-MEM expansion medium (Gibco, USA), supplemented with 10% fetal bovine serum (FBS, Gibco, USA), 0.2 mM L-ascorbic-acid-2-phosphate (ASAP, Sigma-Aldrich, Germany), and 1% penicillin−streptomycin (Pen-Strep, Sigma-Aldrich, Germany). Prior to cell seeding, scaffolds were sterilized in 70 v/v% ethanol for 1 h followed by 30 min under ultraviolet (UV) light. hMSCs were first expanded for 10 days in expansion media at 37 °C in a humidified atmosphere containing 5% CO_2, and then seeded onto scaffolds at a density of 50000 cells/well in 48 well plates. As a positive control for determining the osteogenic potential of the scaffolds, samples were also cultured in media supplemented with osteogenic components (α-MEM + 10% FBS + 0.2 mM ASAP + 1% Pen-Strep + 10 nM dexamethasone+10 mM β-glycerophosphate, Sigma-Aldrich, Germany). At least three samples were tested for each group (i.e., expansion medium and osteogenic medium).

2.9.1. Cell Viability and Morphology Analyses. The metabolic activity of hMSCs was quantified by an Alamar blue assay (ThermoFisher, USA), following the manufacturer's instructions.[25] In order to visualize the cell morphology, scaffolds were first fixed in formalin for 30 min after 1, 7, and 14 days of culturing in expansion media. Samples were permeabilized with 0.2% (v/v) Triton X-100 in phosphate-buffered saline (PBS), followed by incubation with F-actin (1:400; phalloidin-TRITC; Sigma-Aldrich) and 4′,6-diamidino-2-phenylindole (100 ng/mL; DAPI; Sigma-Aldrich). Stained samples were imaged with a confocal laser scanning microscope (Leica SP8X, Germany) and dedicated acquisition software (Leica LASX, Germany).

2.9.2. Osteogenic Potential Evaluation. The osteogenic differentiation of hMSCs was measured using alkaline phosphatase (ALP) at day 7 and day 14 of *in vitro* culture, following a protocol described elsewhere.[21] Briefly, the ALP activity was measured using a conversion of the *p*-nitrophenyl phosphate liquid substrate system (pNPP, Sigma-Aldrich. Germany) and a serial dilution of calf intestinal ALP for the standard curve (Sigma-Aldrich, Germany) in TE-buffer (Tris EDTA buffer). In addition, the calcium concentration was quantified after 21 days using a colorimetric calcium assay kit (Abcam, UK) according to

https://doi.org/10.1021/acsami.2c21256
ACS Appl. Mater. Interfaces 2023, 15, 12735−12749

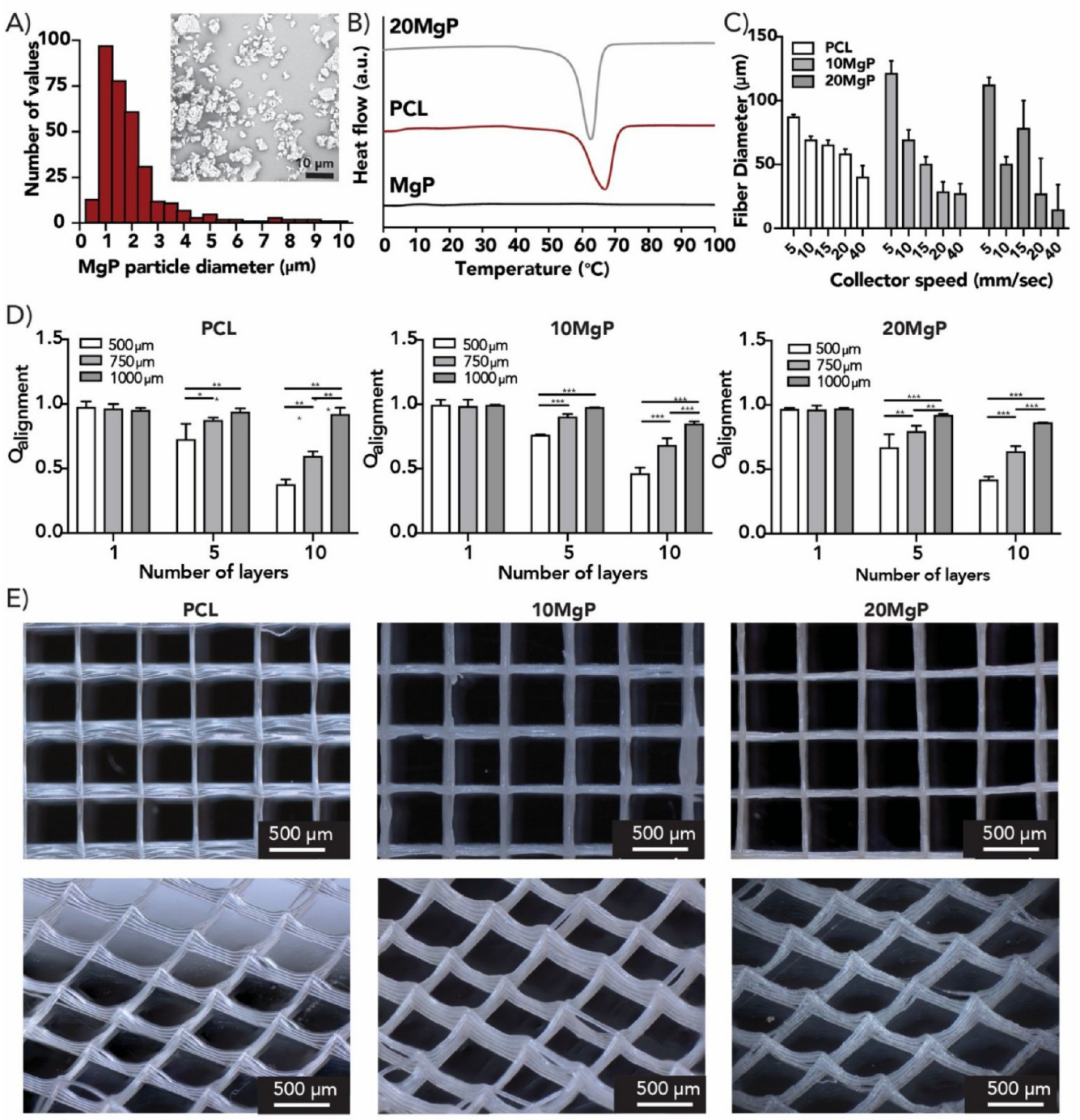

Figure 1. (A) Particle size distribution and morphology analysis of the MgP ceramic powder. (B) Thermal properties of PCL, 10MgP, and 20MgP. (C) Effect of MEW collector speed on fiber diameter. (D) Effect of fiber stacking and fiber spacing on printing accuracy. (E) Representative stereoscopic images of PCL, 10MgP, and 20MgP composite scaffolds with 500 μm fiber spacing and 10 stacked layers.

the manufacturer's instructions. ALP and calcium levels were corrected for DNA content from the same cell lysate used to measure ALP, using a Quan-iT-Picogreen-dsDNA kit (Molecular Probes, Invitrogen, Carlsbad, USA). To determine the calcium concentration after 21 days of culturing, a Calcium Assay Kit (Colorimetric, Abcam ab102505, USA) was used according to the manufacturer's protocol.[26]

2.10. Animal Experiments, Histology, and Immunohistochemistry. The University of Michigan Institutional Animal Care and Use Committee (IACUC, protocol #PRO00008502) approved all animal procedures. In total, 12 male rats (6-week-old male Fischer 344 rats, body weight 300−320 gr) were used for the experiments. The previously established defect dimensions were 3 mm in length × 2 mm in width × 1 mm in height, and the exact dimension of the printed scaffold was press-fitted inside the defect, protected by the defect borders, and then covered by muscles sutured in place. All surgical procedures were carried out under general anesthesia, which was induced with isoflurane (4−5%) inhalation (Piramal Critical Care Inc.) and maintained with isoflurane at 1−3%. After anesthesia, periodontal fenestration defects (3 mm length × 2 mm width × 1 mm height) were surgically generated bilaterally in the rat jaw. The alveolar bone, cementum, and other soft tissue structures were all removed in this procedure. The scaffolds (n = 3/group) were placed inside the defects and tested for their ability to regenerate the periodontium. The animals were humanely euthanized 6-weeks

https://doi.org/10.1021/acsami.2c21256
ACS Appl. Mater. Interfaces 2023, 15, 12735−12749

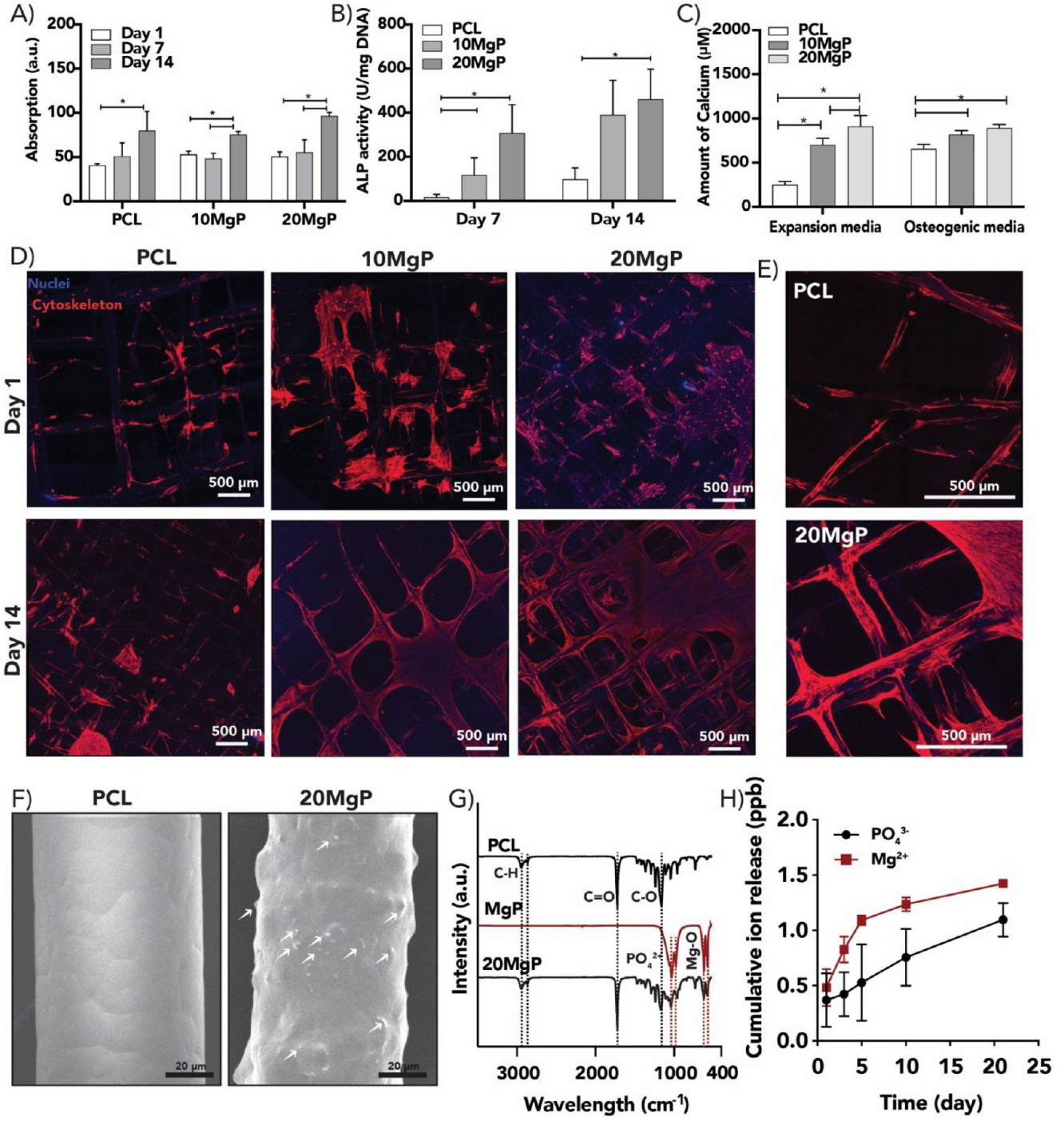

Figure 2. (A) Metabolic activity of hMSCs during 14 days of *in vitro* culture. (B) Alkaline phosphatase (ALP) activity of cells in MEW scaffolds cultured in expansion media. ALP activity levels were normalized to DNA content. (C) Calcium deposition in scaffolds after 21 days of culture in expansion and osteogenic media. (D) Cytoskeleton and nuclei staining of hMSCs in expansion media. (E) Higher magnification of stained hMSCs on PCL and 20MgP scaffolds after 14 days. (F) SEM images of single fibers of PCL and 20MgP (MgP particles identified with white arrows). (G) FTIR analysis of as-printed 20MgP composite scaffolds. (H) Cumulative ion release from 20MgP composite scaffolds upon incubation in Tris-HCl media over 21 days.

postscaffold implantation and the surgical sites fixed in 4 v/v% paraformaldehyde solution before microcomputed tomography (μCT) and histo- and immunological analyses. To simplify, the groups were named empty, 20MgP-na, 20MgP-crsht, and 20MgP-rnd according to the architecture of the graded scaffolds.

2.10.1. Microcomputed Tomography (μCT). A Scanco CT 100 instrument (Scanco Medical AG, Brüttisellen, Switzerland) equipment was used to examine the newly formed bone at the surgical sites. The scan parameters 70 kV, 114 μA monochromatic X-rays, and 25 μm voxel sizes were used to create a 360° rotation. The exposure period was kept to an average of 500 ms per frame on average. For 3D image reconstruction, the Scanco Medical System software was employed. The 3D image was then utilized to trace the original defects circumferentially, which was named the region of interest afterward (ROI). Each sample's ROI was examined for bone volume (BV, mm^3), bone fill (BF %, BV/TV), and tissue mineral density (TMD, $mgHA/cm^3$).[19]

https://doi.org/10.1021/acsami.2c21256
ACS Appl. Mater. Interfaces 2023, 15, 12735−12749

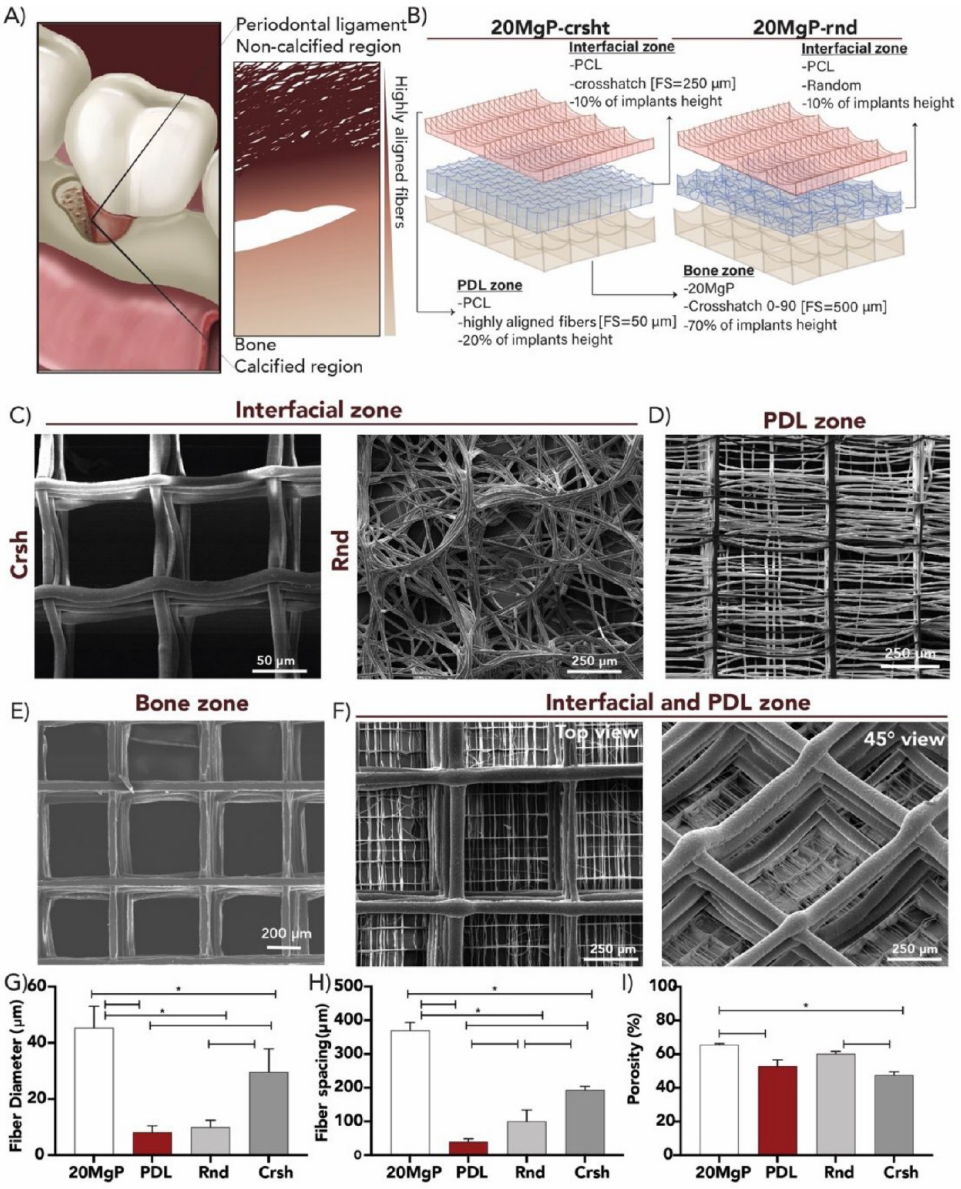

Figure 3. (A) Illustration of the periodontal site and the structure of the bone−PDL interface. (B) Design approach and sequential melt electrowriting strategy of the graded scaffolds (FS = fiber space). Representative SEM images of the (C) crosshatch random structure of electrowritten PCL, (D) highly aligned PCL fibers for the PCL zone, (E) 20MgP fibers for the bone zone, and (F) interfacial crosshatch and PDL zones from top and side views. (G) Fiber diameter, (H) fiber spacing, and (I) porosity at the different zones of the printed graded scaffolds.

2.10.2. Histological Analysis and Immunofluorescence. The harvested samples were decalcified in 10% EDTA for 3 weeks. Following that, the samples were dehydrated in an ascending gradient of ethanol. Afterward, samples were embedded in paraffin. Histological sections of 4 μm were stained with hematoxylin and eosin (HE) and Masson's trichrome (MT). To examine soft and mineralized tissue neoformation, the slides were imaged using a light microscope equipped with a digital camera (Nikon E800, Nikon Corporation).

For immunostaining, the harvested samples were embedded in paraffin and then cut into 4 μm thick sections using a microtome. Sections were dewaxed at 60 °C for 15 min, followed by rehydrating using well-established ethanol gradients. Sections were incubated for 20 min in 3% hydrogen peroxide at RT to decrease the activity of endogenous peroxidase. Sections were incubated (10 min) in 3% bovine serum albumin (BSA) at room temperature to block unspecific binding. They were incubated with antiperiostin (rabbit polyclonal, ab14041, Abcam, Cambridge, MA, USA) (dilution 1:500), anti-osteopontin (mouse monoclonal, ab69498, Abcam) (dilution 1:500), and anti-CEMP1 (rabbit polyclonal, b254947, Abcam) (dilution 1:200) overnight at 4 °C. Subsequently, the sections were incubated with goat antimouse IgG H&L (ab6785, FITC) and goat antirabbit IgG H&L (ab6719, Texas Red, Abcam) (dilution 1:200) for 1 h at room temperature. Cell nuclei were stained with DAPI using Vectashield antifade mounting media. The images were acquired with a microscope (Nikon E800, Nikon Corporation) at 100× magnification.

2.11. Statistical Analysis. All data were represented as means ± standard deviations (SDs), and at least three samples were evaluated for each test. Normality of distribution and equality in variance among groups were evaluated. Statistical analyses were performed using GraphPad prism V9. Assuming anequal sample size of compared groups, a one- or two-way ANOVA with posthoc Tukey's test was performed to compare the means of the different groups. Differences were considered significant at a probability error (p) of $^{*}p < 0.05$ for the printability and mechanical tests and $^{**}p < 0.01$ for animal tests.

https://doi.org/10.1021/acsami.2c21256
ACS Appl. Mater. Interfaces 2023, 15, 12735−12749

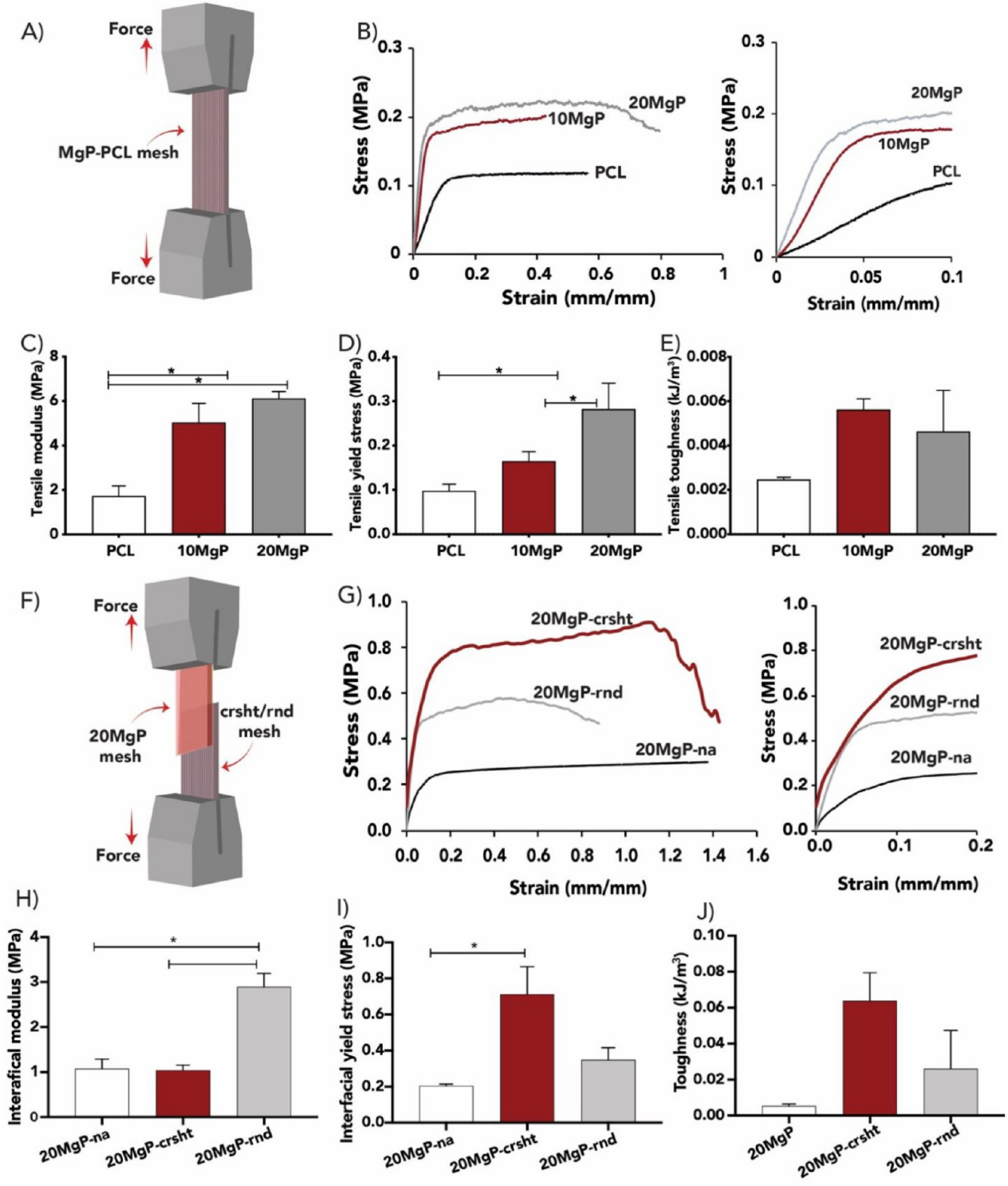

Figure 4. (A) Schematic of testing setup. (B) Representative stress−strain curves of melt electrowritten scaffolds with different MgP concentrations. Determined (C) tensile modulus, (D) tensile yield stress, and (E) tensile toughness of scaffolds with various MgP concentrations. (F) Schematic of tensile setup used for interfacial tests. (G) Representative stress−strain curves of the graded scaffolds with different interfacial architectures and determined (H) interfacial modulus, (I) interfacial yield stress, and (J) interfacial toughness.

3. RESULTS

3.1. Melt Electrowriting of Magnesium Phosphate Based Biomaterial Inks. The ability to melt electrowrite MgP-based biomaterial inks is mainly dependent on the particle size and thermal properties of the compounded polymer. To prevent nozzle clogging, MgP powders were prepared with a monomodal particle distribution with an average particle size of approximately 1 μm (Figure 1A).

In addition, a DSC analysis revealed that melting temperatures ranged from 70 to 80 °C and, more importantly, that the addition of MgP did not significantly alter the melting temperature of PCL (80 °C) (Figure 1B). It was found that although, according to DSC results, the melting point of

https://doi.org/10.1021/acsami.2c21256
ACS Appl. Mater. Interfaces 2023, 15, 12735−12749

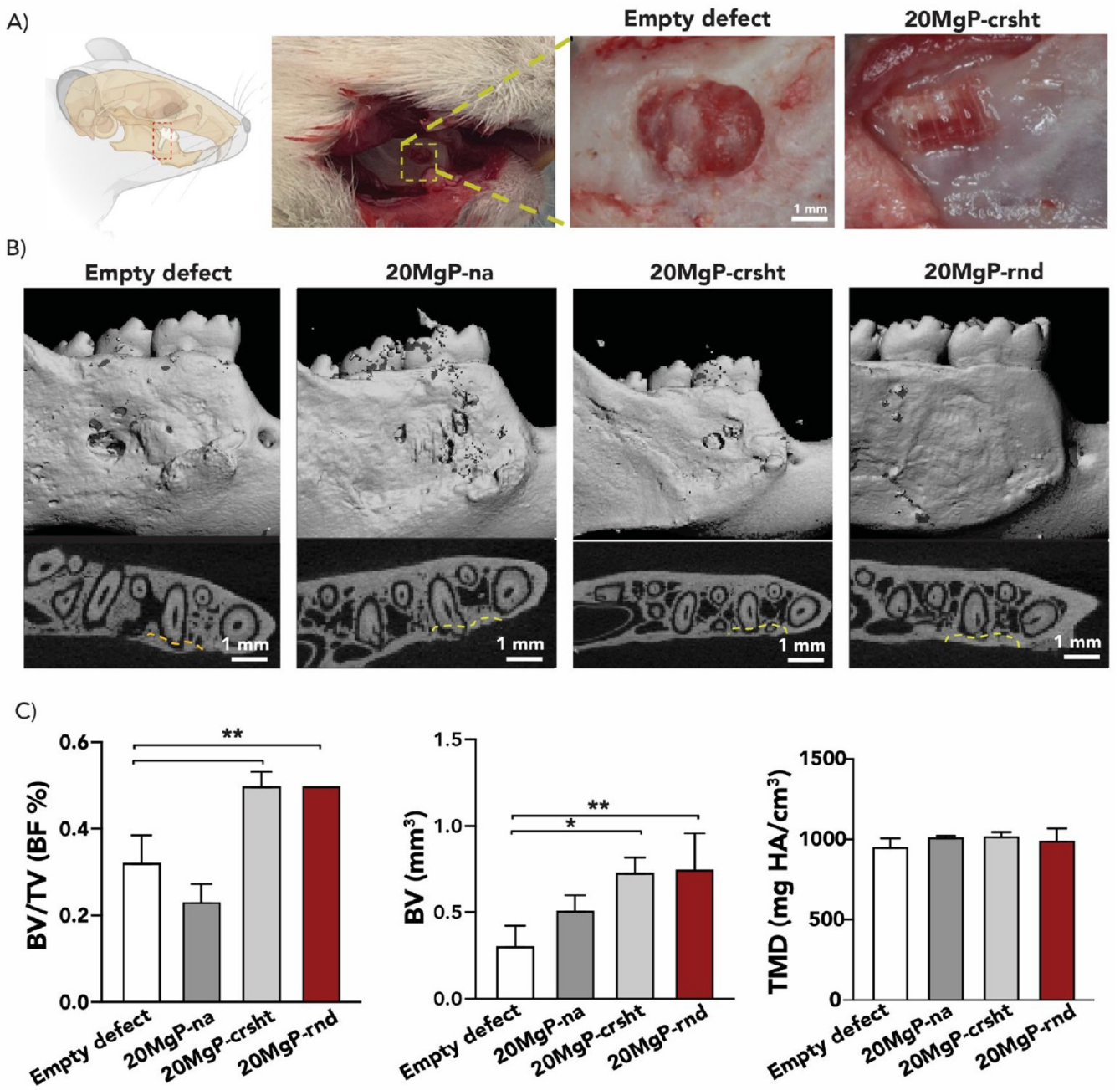

Figure 5. (A) Illustration of the rat mandibular periodontal fenestration model. Photographs of a rat mandible after the incision, flap elevation, creation of the defect, and exposure of the distal root of the mandibular first molar. (B) Representative μCT images of the fenestration defect exposing the distal root of the second molar at 6 weeks. Transverse views in yellow highlight the visual differences between the area and density of bone regenerated within the defect (scale bar = 1 mm). (C) μCT assessments of bone fill and tissue mineral density (TMD) 6 weeks after surgery, within the different groups (**$p < 0.01$).

20MgP composite is close to that of PCL, we could not observe a jet formation below 100 °C. Furthermore, preliminary tests on the influence of key MEW processing parameters (i.e., applied voltage, dispensing pressure, temperature, and collector speed) on stable jet formation (Figure S1A) and fiber collector speed revealed that the temperature and collector speed were the most critical parameters. In general, it was observed that fiber diameters decreased by increasing the collector speed from 5 to 40 mm/s.[27] Additionally, collector speeds of 20 and 40 mm/min resulted in fiber diameters of 15 and 40 μm for PCL and MgP-based composite materials, respectively (Figure 1C). These speeds were selected for further studies on the effect of fiber stacking (Figure 1D). Independent of the MgP content, a decrease in $Q_{alignment}$ was observed with the increasing number of stacked layers (from 1 to 10), and decreasing fiber spacing (from 1000 to 500 μm). Notably, a minimum fiber spacing of 500 μm could be obtained for an MgP content of 20 wt % (Figure 1E and Table S1), without compromising the fiber stacking.

3.2. Osteogenic Properties of MgP-Based Composite Scaffolds. To determine the osteoconductive properties of MgP-based scaffolds, the osteogenic differentiation of seeded human MSCs onto the scaffolds was investigated. First, we confirmed that hMSCs were metabolically active during 21

https://doi.org/10.1021/acsami.2c21256
ACS Appl. Mater. Interfaces 2023, 15, 12735−12749

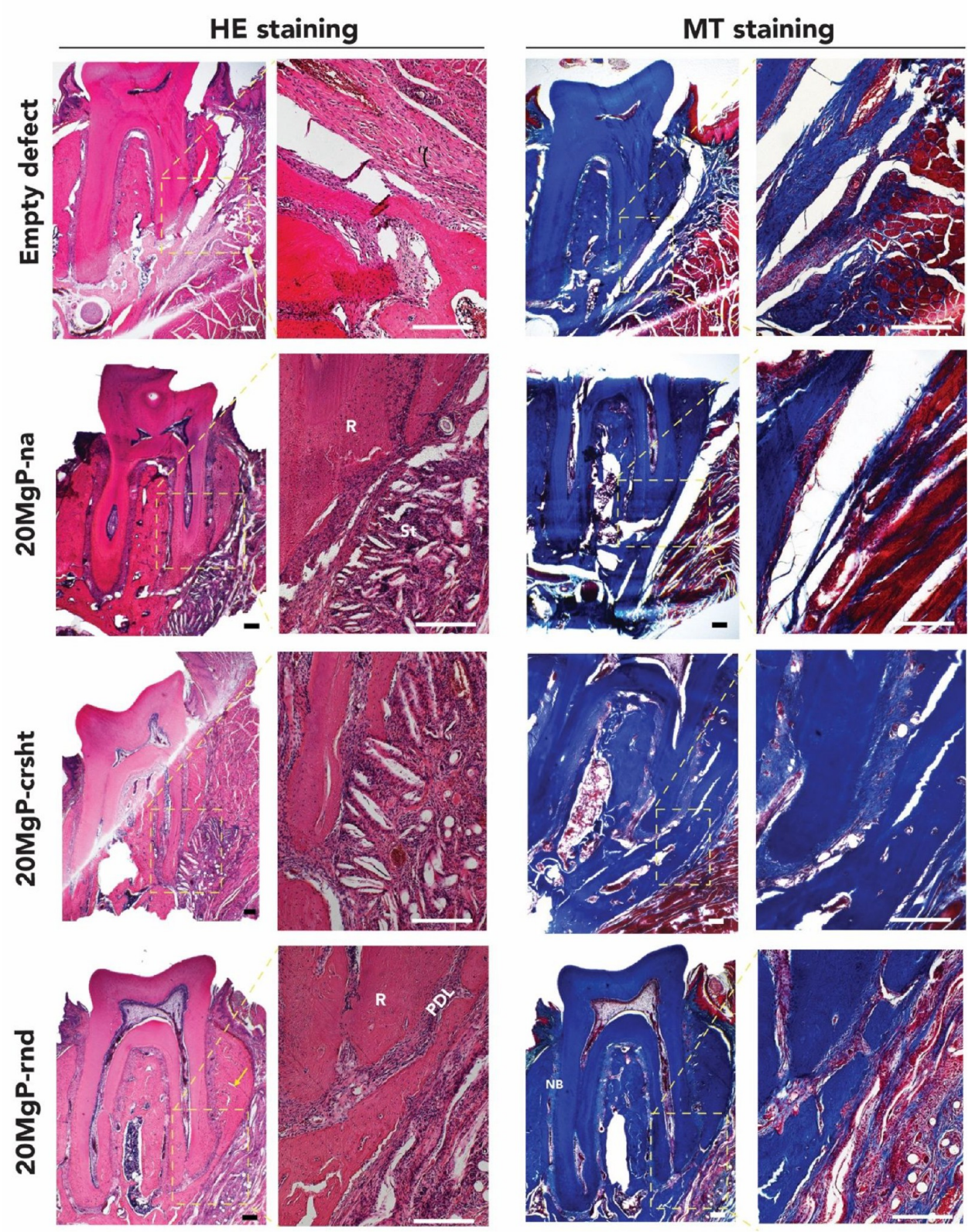

Figure 6. Histological analyses of hematoxylin and eosin (HE) staining and Masson's Trichrome (MT) staining of periodontal defects treated with the distinct graded scaffolds and evaluated after 6 weeks postimplantation (scale bar 100 μm), Abbreviations: NB, new bone; R, root surface; St, Soft tissue.

days of *in vitro* culture (Figure 2A). Then, the ALP activity of the hMSC cells on PCL and MgP-based scaffolds (10MgP and 20MgP) was evaluated in expansion media as a measure of early osteogenic potential (Figure 2B). After 7 days of *in vitro* culture, the ALP activity for 20MgP was almost 20 times higher than that for MgP-free (i.e., PCL) composition. We also observed that the ALP activity of hMSCs cultured on 20MgP increased from 306.93 to 460.27 I U/mg DNA between 7 and

https://doi.org/10.1021/acsami.2c21256
ACS Appl. Mater. Interfaces 2023, 15, 12735−12749

14 days (an increase of 150%), while the ALP activity of hMSCs cultured on PCL was 97.57 U/mg DNA after 14 days. Furthermore, the amount of calcium deposition on the prepared scaffolds was assessed. Calcium deposited on 20 MgP was 1.3 and 3.6 times higher than those on 10MgP and PCL, respectively (Figure 2C). Moreover, no significant differences in calcium deposition of MgP-based scaffolds cultured in expansion and osteogenic media were observed (Figure 2C), which confirms the osteoconductive properties of MgP-based scaffolds. Although these findings corroborate our previous findings on the osteopromotive properties of extruded printed MgP based scaffolds,[22] these results are particularly impressive since the content of MgP used here was only 20 wt %, while in previous efforts the content was 70 wt %.

Furthermore, an improved cell attachment and a more homogeneous distribution were noted when comparing MgP-based scaffolds with their neat PCL counterparts (Figure 2D). Higher magnification confocal images suggested a potentially higher level of cell-secreted matrix components on the 20MgP-based scaffolds than on PCL scaffolds (Figure 2E). To further understand the osteoconductive properties of the MgP-based scaffolds, the presence, distribution, and release of ions (Mg^{2+} and PO_4^{3-}) from PCL fibers were analyzed. SEM (XFigure 2F) and EDX (Figure S1) analyses revealed that MgP ceramic particles were successfully incorporated into the PCL matrix. FTIR analyses performed on printed MgP-based fibers (Figure 2G) confirmed the incorporation of ceramic particles. The peaks corresponding to Mg^{2+} and PO_4^{3-} were detected in the spectrum of 20MgP fibers. Lastly, a burst release of Mg^{2+} and PO_4^{3-} ions was noted during the first 5 days in an aqueous solution, followed by a gradual and sustained release of these ions up to 21 days (Figure 2H).

3.3. Melt Electrowriting of Graded Scaffolds. MEW graded scaffolds were designed to recreate the spatial changes in matrix composition and organization observed in the native PDL−bone interface (Figure 3A,B). In particular, a three-zoned scaffold with different porous boxed-shaped architectures and material compositions was successfully fabricated by melt electrowriting (Figure 3).

To maximize the adhesion between the bone zone (20MgP composite) and PDL scaffold zone (PCL), two different interfacial architectures, crosshatch 0/90 (crsht, Figure 3C) and random (rnd, Figure 3C) were investigated. The representative SEM images of PDL and bone zones are shown in Figure 3D,E. An SEM analysis confirmed that, independent of the interface architecture explored, the as-fabricated scaffolds showed consistent and reproducible printability (Figure 3F). The fiber diameter of the bone zone is 45.3 μm for 20MgP, and that of the PDL zone is 8.2 μm for PCL (Figure 3G). As such, the fiber diameters of the interfacial zone are 9.9 and 29.6 μm for rnd and crsht, respectively. The difference in the fiber diameter is due to various fabrication (MEW) parameters. The fiber spacing of 20MgP deviated to 369.21 μm from the design of 500 μm, while the fiber spacing of PDL deviated to 39.48 μm for the 50 μm scaffold (Figure 3H). This resulted in porosity values for all three regions above 50% (Figure 3I). In particular, the porosities of the bone and PDL zones were 65.6% and 52.8%, respectively.

3.4. Mechanical Characterization of Melt Electrowritten Scaffolds. We next investigated whether the incorporation of MgP particles or interface architecture could improve the tensile properties of the developed graded scaffolds (Figure 4A). All investigated scaffolds showed similar stress−strain behaviors (Figure 4B). The increase in MgP content from 10 to 20 wt % resulted in an increase in both the tensile modulus and tensile yield stress. For instance, the tensile modulus and tensile yield stress of 20MgP increased approximately 3.5 and 3.1 times in comparison to the PCL scaffold, respectively (Figure 4C,D). Incorporation of MgP into the PCL matrix resulted in an increase of approximately 2 times in tensile toughness; however, no significant differences were noticed between 10MgP and 20MgP scaffolds (Figure 4E).

Furthermore, an interfacial tensile test between the different zones of the scaffolds (i.e., bone and PDL zones) revealed the strong bond between two different phases of the scaffold, as compared to the delamination of the scaffolds with a single zone (Figure 4F). Interestingly, the interfacial modulus of 20MgP-crsht was almost 2.5 times higher than that of 20MgP-na (Figure 4H), while the interfacial yield strength of 20MgP-crsht was 3 times greater than that of 20MgP-na (Figure 4I). Moreover, the interfacial toughnesses of 20MgP-crsht and 20MgP-rnd were 0.06 ± 0.01 and 0.02 ± 0.01 kJ m^{-3}, respectively (Figure 4J).

3.5. Microcomputed Tomographic (μCT) Analysis of Regenerated Tissue. The ability of the designed scaffolds to support the growth of new tissues *in vivo* was tested using a well-established periodontal fenestration defect model in rat mandible[20] (Figure 5A).

Based on a μCT examination, the graded scaffold group exhibited considerable improvement in alveolar bone healing following surgery (Figure 5B). Quantitative μCT measurements showed that bone volume and bone fill in groups with interfacial layers were approximately 42% greater than those of the control (sham) and 25% than those with no interfacial layer (Figure 5C and Figure S2). The group with interfacial layers achieved nearly full bone repair compared to partial bone repair in the control sham and the group with no interfacial layer by 6 weeks, leaving a visible remaining bone defect on the buccal surface and uncovered distal root (Figure 5B). Compared to these groups, the 20MgP-rnd group had a higher rate of complete bone fill, which bridged the entire lesion region, indicating active osteogenesis. The newly formed bone in the interfacial group displayed more significant bone fill and was less distinct from the adjacent native bone, suggesting a higher bone bridging than the other groups.

The histological findings underscore the multitissue regeneration via both structural and compositional guidance of graded scaffolds toward periodontium regeneration (Figure 6).

HE and MT staining after 6 weeks of *in vivo* implantation showed distinctive yet integrated bone and ligament tissues that form in the graded scaffolds with a random interface architecture. The presence of the interfacial zone in the 20MgP-rnd group was sufficient to maintain the PDL zone and restrict the fibrous tissue formation confined toward the intended PDL zone mimicking the natural PDL area. Interestingly, the random interfacial layer compared to the crosshatch pattern formed a better integrated transition from the bone to PDL-like tissue. This difference can be attributed to the smaller fiber spacing of the random interface layer (20MgP-rnd) compared to the 20MgP-crsht group. Moreover, the PDL-like tissue was formed into the mineralized bone. It is worth mentioning that the scaffold with no interfacial layer showed more soft tissue formation in the PDL−bone interface.

https://doi.org/10.1021/acsami.2c21256
ACS Appl. Mater. Interfaces 2023, 15, 12735−12749

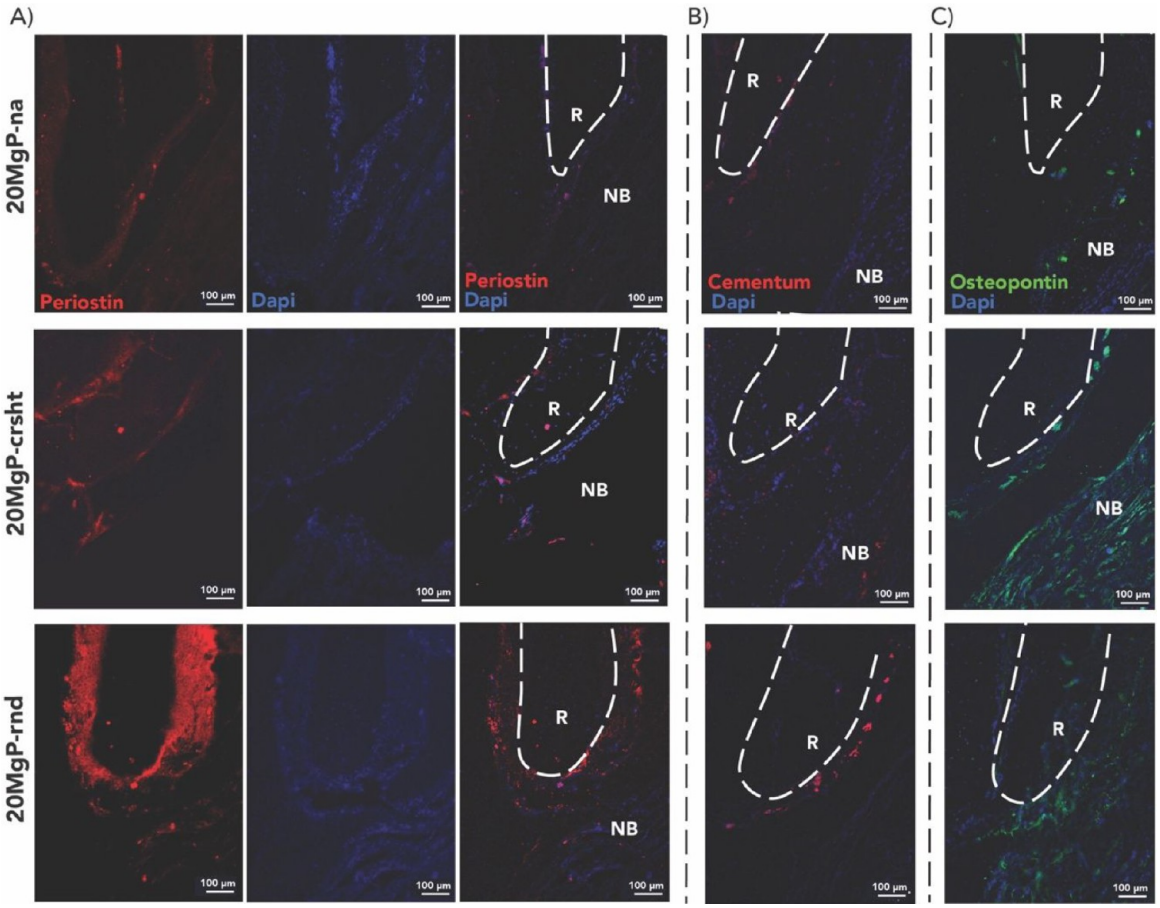

Figure 7. (A) Immunofluorescence staining for the expression of periostin at the PDL zone. Representative mesiodistal cross-section at the first lower molar region. Texas Red showing positive periostin immunolabeling and DAPI for cell nuclei staining. Merged colors on the right side with postprocessing background reduction. (100× magnification; scale bars 100 μm). Abbreviations: NB, new bone; R, Root surface. Immunofluorescence staining for the expression of (B) cementum and (C) osteopontin at the PDL zone. Representative mesiodistal cross-section at the first lower molar region. Texas Red and fluorescein (FTIC) showed positive cementum and osteopontin immunolabeling, respectively. The two markers were merged with DAPI images for cell nuclei staining (100× magnification; scale bars 100 μm). Abbreviations: NB, new bone; R, Root surface.

3.6. Immunofluorescence Staining for the Expression of Periostin, Osteopontin, and Cementum at the PDL Zone. The graded scaffolds 20MgP-crsht and 20MgP-rnd appear to have a better periodontal ligament regeneration and newly formed bone support in the employed defect model with superior potential in the 20MgP-rnd group compared to 20MgP-na. The expressions of CEMP1, osteopontin, and periostin were immunolabeled. The early marker for periodontal regeneration is expressed by periostin protein, which is distinguished for 20MgP-rnd. Also, 20MgP-rnd exhibited a higher cementum protein 1 (CEMP1) expression along with enhanced immunolabeling for osteopontin and periostin compared to 20MgP-na and 20MgP-crsht (Figure 7 and Figure S2). The osteopontin was also expressed for all the tested groups except for 20MgP-rnd; osteopontin is expressed around the root of the tooth.

4. DISCUSSION

In this investigation, we described the development of a graded melt electrowritten scaffold, which was composed of an osteoconductive ceramic-based biomaterial for the bone zone and highly aligned polymer fibers for the PDL zone. The embedded MgP bioceramics were able to promote bone regeneration and simultaneous degradation of the scaffolds *in vivo*. Similar scaffolds, based on MEW processing, previously showed potential for application in periodontal repair procedures, and the inclusion of low concentrations of bioceramics, i.e., hydroxyapatite or fluorapatite, was demonstrated to enhance bone regeneration.[28−30] While this application of MEW enabled the generation of thin ceramic-coated PCL fibers with diameters ranging from 20 to 50 μm,[30,31] it did result in a burst release of osteogenic ions from the PCL fibers.[20] In order to overcome this, the polymer was compounded with bioceramics. This strategy showed promising results, although only composites with a bioceramic content of lower than 10 wt % could be successfully generated, which resulted in limited osteoinductivity properties due to masking of the bioceramics by the polymer.[32]

In this study, processing of a MgP biomaterial ink with 20 wt % of ceramic content (20MgP) was successfully achieved at 100 °C: however, only after a thermal exposure of 6 h at 140 °C. This is probably related to the preprocessing of PCL, which affects its crystallinity and will, in turn, facilitate the extrusion of 20MgP. Further, it was confirmed that the composition was not cytotoxic and promotes better osteogenic differentiation of mesenchymal stem cells compared to bare PCL or the composite containing 10 wt % ceramics. The increased osteogenic potential is very likely related to the

https://doi.org/10.1021/acsami.2c21256
ACS Appl. Mater. Interfaces 2023, 15, 12735−12749

higher ceramic content and the consequent higher release of osteogenic ions (Mg^{2+} and PO_4^{3-}) from the MgP ceramic phase.[33−36] In a previous study, we showed abundant calcium (200 μM) deposition on the extrusion-based printed PCL scaffolds with 70 wt % of MgP after 21 days of *in vitro* culture.[22] The calcium deposited on the 20MgP MEW scaffolds is, however, 5 times higher than that in the previous study. This underscores the synergistic effect between the osteoinductive ions and the high surface area provided by the small fiber diameters of the MEW scaffolds. Moreover, the network of small-diameter fibers does also better resemble the extracellular matrix microstructure of the native bone.[37−39] This underscores the synergistic effect between the osteoinductive ions and the high surface area provided by the small polymeric fiber diameters of the MEW scaffolds. Moreover, the network of small-diameter fibers better resembles the extracellular matrix (ECM) microstructure of the native bone.[18,19] Furthermore, according to our findings, a more homogeneous distribution of the MgP particles can be achieved by extruding the formulated composite paste at high temperature prior to actual printing of the scaffolds.

In addition, the tensile mechanical properties of the 20MgP scaffolds have the highest elastic modulus and strength among the tested groups. This is probably explained by the fact that the addition of 20 wt % of MgP allows for a more uniform dispersion and interaction with the PCL matrix, without the introduction of defects.[40] The tensile yield stress of the 70 wt % MgP based scaffold generated by extrusion was 1.5 MPa,[22] while the melt electrowritten 20MgP scaffolds have a tensile yield stress of 3 MPa. After establishing the MEW processing of the 20MgP for the bone region, graded scaffolds were generated with two different interfacial zone architectures and highly aligned fibers for the PDL region. Evaluation of the interfacial tensile properties revealed that randomly oriented fibers (20MgP-rnd) provided better mechanical integration between the two regions than 20MgP-crsht. This is likely due to the fact that the randomly oriented fibers have more contact points with the PDL scaffold than those in the graded scaffolds.

Recently, our group reported on a graded scaffold whereby the bone region was comprised of fluorinated calcium phosphate (F/CaP)-coated MEW fibers, while the PDL region featured highly aligned fibers. Positive effects of aligned PCL fibers on the formation of PDL tissue have been previously reported.[41−43] Remarkably, *in vivo* findings in the current study revealed that these tissue-specific scaffolds led to formation of PDL fibers perpendicularly oriented to the root surface and integrated in the newly formed bone surface.[19] Despite the promising outcomes, the necessity for postprocessing in order to obtain the bioceramic (F/CaP) coating to enhance the bioactivity of the scaffolds can pose difficulties for clinical translation. This study overcomes the need for an additional step, as we hypothesize that a osteoconductive scaffold with a graded blend of MgP bioceramics and polycaprolactone (PCL) with a tissue-specific, stable interfacial zone and structural properties can facilitate a long-term bone-to-ligament regeneration. In line with the present findings, Staples et al. evaluated a biphasic scaffold generated with MEW comprised of two integrated compartments for bone and PDL.[44] The PDL compartment consisted of a parallel fiber organization creating 100 μm spaced channels, while the bone compartment constituted a gradient of pore sizes ranging between 200 and 1200 μm. Although the scaffold resembled the tooth−ligament interface, the lack of osteoinductive factors might explain the limited new bone formation observed in that study.

In this study, the composite scaffolds were evaluated in an *in vivo* periodontal fenestration defect model. This well-established *in vivo* defect model allows determination of the ability of the scaffold to support the coordinated neotissue formation of soft and hard periodontal tissues.[19] Notably, our scaffolds showed the ability to induce simultaneous regeneration of bone and PDL. The enhanced repair in groups treated with a composite scaffold compared to other groups is apparent due to increased immunolabeling for CEMP1 expression, osteopontin, and periostin. Of note, CEMP1 is a cementum component limited to cementoblasts and their progenitors. The apparently equal expression among the tested groups, as indicated by the immunolabeling, demonstrates that the proposed scaffolds do not impair the ability of neotissue formation, since the overexpression of CEMP1 downregulates the periodontal ligament cell marker.[45] Meanwhile, osteopontin, also known as bone sialoprotein I, regulates mineralization *in vitro* and *in vivo* and is a crucial factor in the extracellular matrix of both cementum and alveolar bone.[46] Lastly, periostin, in turn, has successfully been used as a periodontal regeneration marker, since it is a secreted adhesion molecule highly expressed in the periosteum and periodontal ligament, playing a vital role in the regeneration of periodontal ligament and alveolar bone.[47]

Collectively, our findings demonstrate the benefit of a multilayered, composite scaffold for enhanced bone formation, while also reflecting the natural process of PDL formation. The beneficial effect can be attributed to the compositional gradients and the structural organization of the scaffolds. The presence of an interfacial layer with a lower porosity confines the tissue-specific regenerative environment and subsequently supports simultaneous regeneration of both the bone and PDL tissues. The combined osteopromotive and ligament-regenerative properties of the developed scaffolds can also support stable mechanical integration. Collectively, MEW-fabricated scaffolds having compositionally and structurally tailored zones exhibit a good mimicry of the periodontal complex, with excellent regenerative capacity and great potential as a defect-specific treatment strategy.

5. CONCLUSIONS

In summary, the as-developed graded composite melt electrowritten scaffolds showed great potential to regenerate the PDL−bone interface. Structurally and compositionally graded scaffolds were successfully fabricated by MEW in a one-step printing procedure and by combining two biomaterial inks, a flexible, osteoconductive biomaterial ink based on MgP and a PCL ink. The addition of MgP increased the tensile properties of PCL. The tensile modulus of 20MgP increased 3 times compared to PCL alone. Additionally, the relatively high content (20 wt %) of MgP bioceramics incorporated into the PCL matrix supported *in vitro* mesenchymal stem cell differentiation toward the osteoblastic lineage and *in vivo* bone regeneration, while the highly aligned PCL fibers induced PDL regeneration. To ensure the mechanical stability, PCL fibers with a random architecture were printed as interfacial zones. The *in vivo* results confirmed that graded scaffolds with the random architecture interfacial zone allowed for coordinated bone and periodontal tissue regeneration within their respective zones.

https://doi.org/10.1021/acsami.2c21256
ACS Appl. Mater. Interfaces 2023, 15, 12735−12749

■ ASSOCIATED CONTENT

Supporting Information

The Supporting Information is available free of charge at https://pubs.acs.org/doi/10.1021/acsami.2c21256.

Characterization of MEW MgP-20 shown in detail as well as its composition and immunofluorescence staining for the expression of periostin at the PDL zone for the empty defects (PDF)

■ AUTHOR INFORMATION

Corresponding Authors

Marco C. Bottino − *Department of Cariology, Restorative Sciences, and Endodontics, School of Dentistry and Department of Biomedical Engineering, College of Engineering, University of Michigan, Ann Arbor, Michigan 48104, United States;* orcid.org/0000-0001-8740-2464; Email: mbottino@umich.edu

Jos Malda − *Department of Orthopaedics, University Medical Center Utrecht, Utrecht University, Utrecht 3508 GA, The Netherlands; Regenerative Medicine Center Utrecht, Utrecht 3584 CT, The Netherlands; Department of Clinical Sciences, Faculty of Veterinary Medicine, Utrecht University, Utrecht 3553, The Netherlands;* orcid.org/0000-0002-9241-7676; Email: J.Malda@umcutrecht.nl

Authors

Nasim Golafshan − *Department of Orthopaedics, University Medical Center Utrecht, Utrecht University, Utrecht 3508 GA, The Netherlands; Regenerative Medicine Center Utrecht, Utrecht 3584 CT, The Netherlands*

Miguel Castilho − *Department of Orthopaedics, University Medical Center Utrecht, Utrecht University, Utrecht 3508 GA, The Netherlands; Orthopaedic Biomechanics, Department of Biomedical Engineering and Institute for Complex Molecular Systems, Eindhoven University of Technology, Eindhoven 5612 AE, The Netherlands;* orcid.org/0000-0002-4269-5889

Arwa Daghrery − *Department of Restorative Dental Sciences, School of Dentistry, Jazan University, Jazan 45142, Kingdom of Saudi Arabia; Department of Cariology, Restorative Sciences, and Endodontics, School of Dentistry, University of Michigan, Ann Arbor, Michigan 48104, United States*

Morteza Alehosseini − *Technical University of Denmark, Department of Health Technology, Lyngby 2800 Kgs, Denmark*

Tom van de Kemp − *Department of Orthopaedics, University Medical Center Utrecht, Utrecht University, Utrecht 3508 GA, The Netherlands; Regenerative Medicine Center Utrecht, Utrecht 3584 CT, The Netherlands*

Konstantinos Krikonis − *Department of Orthopaedics, University Medical Center Utrecht, Utrecht University, Utrecht 3508 GA, The Netherlands; Regenerative Medicine Center Utrecht, Utrecht 3584 CT, The Netherlands*

Mylene de Ruijter − *Department of Orthopaedics, University Medical Center Utrecht, Utrecht University, Utrecht 3508 GA, The Netherlands; Regenerative Medicine Center Utrecht, Utrecht 3584 CT, The Netherlands*

Renan Dal-Fabbro − *Department of Cariology, Restorative Sciences, and Endodontics, School of Dentistry, University of Michigan, Ann Arbor, Michigan 48104, United States;* orcid.org/0000-0002-4125-8441

Alireza Dolatshahi-Pirouz − *Technical University of Denmark, Department of Health Technology, Lyngby 2800 Kgs, Denmark*

Sarit B. Bhaduri − *Department of Mechanical, Industrial and Manufacturing Engineering, University of Toledo, Toledo, Ohio 43606, United States; EEC Division, Directorate of Engineering, The National Science Foundation, Alexandria, Virginia 22314, United States*

Complete contact information is available at: https://pubs.acs.org/10.1021/acsami.2c21256

Author Contributions

N.G. and M.C. contributed equally.

Notes

The authors declare no competing financial interest.

■ ACKNOWLEDGMENTS

M.C. and J.M. acknowledge financial support from the Regenerative Medicine Crossing Borders and powered by Health Holland, Top Sector Life Sciences & Health, The Netherlands. M.C. is also grateful for financial support from the Reprint project (OCENW.XS5.161) by The Netherlands Organization for Scientific Research. M.C.B. acknowledges the National Institutes of Health (NIH−National Institute of Dental and Craniofacial Research, grant R01DE031476). The content is solely the responsibility of the authors and does not necessarily represent the official views of the NIH and the National Science Foundation (NSF). We acknowledge the use of Adobe Illustrator (version 27.0) and Adobe Photoshop (version 24.0) to prepare Figures 3,A,B and 4A,F and Biorender (BioRender.com) to generate the illustration presented as Figure 5A. The figure presented in the table of contents and abstract was also generated by combining the aforementioned softwares. These figures are original and do not infringe on the copyright of others.

■ REFERENCES

(1) Lei, T.; Zhang, T.; Ju, W.; Chen, X.; Heng, B. C.; Shen, W.; Yin, Z. Biomimetic Strategies for Tendon/Ligament-to-Bone Interface Regeneration. *Bioact Mater.* **2021**, *6* (8), 2491.

(2) Yang, P. J.; Temenoff, J. S. *Engineering Orthopedic Tissue Interfaces.* www.liebertonline.com=ten.

(3) Park, C. H.; Rios, H. F.; Jin, Q.; Bland, M. E.; Flanagan, C. L.; Hollister, S. J.; Giannobile, W. v. Biomimetic Hybrid Scaffolds for Engineering Human Tooth-Ligament Interfaces. *Biomaterials* **2010**, *31* (23), 5945−5952.

(4) Criscenti, G.; Longoni, A.; di Luca, A.; de Maria, C.; van Blitterswijk, C. A.; Vozzi, G.; Moroni, L. Triphasic Scaffolds for the Regeneration of the Bone-Ligament Interface. *Biofabrication* **2016**, *8* (1), 015009.

(5) Liang, Y.; Luan, X.; Liu, X. Recent Advances in Periodontal Regeneration: A Biomaterial Perspective. *Bioact Mater.* **2020**, *5* (2), 297−308.

(6) Lee, C. H.; Hajibandeh, J.; Suzuki, T.; Fan, A.; Shang, P.; Mao, J. J. Three-Dimensional Printed Multiphase Scaffolds for Regeneration of Periodontium Complex. *Tissue Eng. Part A* **2014**, *20* (7−8), 1342−1351.

(7) Eke, P. I.; Wei, L.; Borgnakke, W. S.; Thornton-Evans, G.; Zhang, X.; Lu, H.; McGuire, L. C.; Genco, R. J. Periodontitis Prevalence in Adults ≥ 65 Years of Age, in the USA. *Periodontol 2000* **2016**, *72* (1), 76.

(8) WHO. https://www.euro.who.int/en/health-topics/disease-prevention/oral-health/data-and-statistics. https://www.euro.who.int/en/health-topics/disease-prevention/oral-health/data-and-statistics.

(9) Amar, S.; Chung, K. M.; Nam, S. H.; Karatzas, S.; Myokai, F.; van Dyke, T. E. Markers of Bone and Cementum Formation Accumulate in Tissues Regenerated in Periodontal Defects Treated with Expanded Polytetrafluoroethylene Membranes. *J. Periodontal Res.* **1997**, *32* (1), 148−158.
(10) Dai, J.; Si, J.; Ouyang, N.; Zhang, J.; Wu, D.; Wang, X.; Shen, G. Dental and Periodontal Phenotypes of Dlx2 Overexpression in Mice. *Mol. Med. Rep* **2017**, *15* (5), 2443−2450.
(11) Bottino, M. C.; Thomas, V.; Schmidt, G.; Vohra, Y. K.; Chu, T. M. G.; Kowolik, M. J.; Janowski, G. M. Recent Advances in the Development of GTR/GBR Membranes for Periodontal Regeneration—A Materials Perspective. *Dental Materials* **2012**, *28* (7), 703−721.
(12) Liu, J.; Ruan, J.; Weir, M. D.; Ren, K.; Schneider, A.; Wang, P.; Oates, T. W.; Chang, X.; Xu, H. H. K. Periodontal Bone-Ligament-Cementum Regeneration via Scaffolds and Stem Cells. *Cells* **2019**, *8* (6), 537.
(13) Bottino, M. C.; Pankajakshan, D.; Nör, J. E. Advanced Scaffolds for Dental Pulp and Periodontal Regeneration. *Dent Clin North Am.* **2017**, *61* (4), 689−711.
(14) *Analysis of the in vitro degradation and the in vivo tissue response to bi-layered 3D-printed scaffolds combining PLA and biphasic PLA/bioglass components - Guidance of the inflammatory response as basis for osteochondral regeneration | Elsevier Enhanced Reader*. https://reader.elsevier.com/reader/sd/pii/S2452199X16300555X?token=D2D5DA14B4774596F1F9E3D579B9860FF37C15FD3A1735459CEDA364E12CA2B5EDE989B9647A4163BC771055B9BD53D9&originRegion=eu-west-1&originCreation=20211210161747 (accessed 2021-12-10).
(15) Castilho, M.; Mouser, V.; Chen, M.; Malda, J.; Ito, K. Bi-Layered Micro-Fibre Reinforced Hydrogels for Articular Cartilage Regeneration. *Acta Biomater* **2019**, *95*, 297−306.
(16) *Stratified scaffold design for engineering composite tissues | Elsevier Enhanced Reader*. https://reader.elsevier.com/reader/sd/pii/S1046202315001462?token=1A0552B940ECD9EFE9AC39AF5E2169327EEAF595EB1DE5287889C1686EE9B6FACEAF5E58C24B0C216935B9174A5D3FF8&originRegion=eu-west-1&originCreation=20211210162201 (accessed 2021-12-10).
(17) Dubey, N.; Ferreira, J. A.; Daghrery, A.; Aytac, Z.; Malda, J.; Bhaduri, S. B.; Bottino, M. C. Highly Tunable Bioactive Fiber-Reinforced Hydrogel for Guided Bone Regeneration. *Acta Biomater* **2020**, *113*, 164.
(18) Samavedi, S.; Vaidya, P.; Gaddam, P.; Whittington, A. R.; Goldstein, A. S. Electrospun Meshes Possessing Region-Wise Differences in Fiber Orientation, Diameter, Chemistry and Mechanical Properties for Engineering Bone-Ligament-Bone Tissues. *Biotechnol. Bioeng.* **2014**, *111* (12), 2549−2559.
(19) Daghrery, A.; Ferreira, J. A.; Xu, J.; Golafshan, N.; Kaigler, D.; Bhaduri, S. B.; Malda, J.; Castilho, M.; Bottino, M. C. Tissue-Specific Melt Electrowritten Polymeric Scaffolds for Coordinated Regeneration of Soft and Hard Periodontal Tissues. *Bioact Mater.* **2023**, *19*, 268−281.
(20) Daghrery, A.; Ferreira, J. A.; de Souza Araújo, I. J.; Clarkson, B. H.; Eckert, G. J.; Bhaduri, S. B.; Malda, J.; Bottino, M. C. A Highly Ordered, Nanostructured Fluorinated CaP-Coated Melt Electrowritten Scaffold for Periodontal Tissue Regeneration. *Adv. Healthc Mater.* **2021**, *10* (21), 2101152.
(21) Golafshan, N.; Willemsen, K.; Kadumudi, F. B.; Vorndran, E.; Dolatshahi-Pirouz, A.; Weinans, H.; van der Wal, B. C. H.; Malda, J.; Castilho, M. 3D-Printed Regenerative Magnesium Phosphate Implant Ensures Stability and Restoration of Hip Dysplasia. *Adv. Healthc Mater.* **2021**, *10* (21), 2101051.
(22) Golafshan, N.; Vorndran, E.; Zaharievski, S.; Brommer, H.; Kadumudi, F. B.; Dolatshahi-Pirouz, A.; Gbureck, U.; van Weeren, R.; Castilho, M.; Malda, J. Tough Magnesium Phosphate-Based 3D-Printed Implants Induce Bone Regeneration in an Equine Defect Model. *Biomaterials* **2020**, *261*, 120302.
(23) Kadumudi, F. B.; Jahanshahi, M.; Mehrali, M.; Zsurzsan, T.-G.; Taebnia, N.; Hasany, M.; Mohanty, S.; Knott, A.; Godau, B.; Akbari, M.; Dolatshahi-Pirouz, A. A Protein-Based, Water-Insoluble, and Bendable Polymer with Ionic Conductivity: A Roadmap for Flexible and Green Electronics. *Advanced Science* **2019**, *6* (5), 1801241.
(24) Braham, M. V. J.; Minnema, M. C.; Aarts, T.; Sebestyen, Z.; Straetemans, T.; Vyborova, A.; Kuball, J.; Oner, F. C.; Robin, C.; Alblas, J. Cellular Immunotherapy on Primary Multiple Myeloma Expanded in a 3D Bone Marrow Niche Model. *OncoImmunology* **2018**, *7*, e1434465.
(25) Rampersad, S. N. Multiple Applications of Alamar Blue as an Indicator of Metabolic Function and Cellular Health in Cell Viability Bioassays. *Sensors (Basel)* **2012**, *12* (9), 12347.
(26) de Oliveira, A. A.; Priviero, F.; Tostes, R. C.; Webb, R. C.; Nunes, K. P. Dissecting the Interaction between HSP70 and Vascular Contraction: Role of [Formula: See Text] Handling Mechanisms. *Sci. Rep* **2021**, *11* (1)1420.
(27) Castilho, M.; Feyen, D.; Flandes-Iparraguirre, M.; Hochleitner, G.; Groll, J.; Doevendans, P. A. F.; Vermonden, T.; Ito, K.; Sluijter, J. P. G.; Malda, J. Melt Electrospinning Writing of Poly-Hydroxymethylglycolide-Co-ε-Caprolactone-Based Scaffolds for Cardiac Tissue Engineering. *Adv Healthcare Materials* **2017**, *6*, 1700311.
(28) Kade, J. C.; Dalton, P. D. Polymers for Melt Electrowriting. *Adv. Healthc Mater.* **2021**, *10* (1), 2001232.
(29) Abbasi, N.; Hamlet, S.; Dau, V. T.; Nguyen, N. T. Calcium Phosphate Stability on Melt Electrowritten PCL Scaffolds. *Journal of Science: Advanced Materials and Devices* **2020**, *5* (1), 30−39.
(30) Eichholz, K. F.; von Euw, S.; Burdis, R.; Kelly, D. J.; Hoey, D. A. Development of a New Bone-Mimetic Surface Treatment Platform: Nanoneedle Hydroxyapatite (NnHA) Coating. *Adv. Healthc Mater.* **2020**, *9* (24), 2001102.
(31) Poh, P. S. P.; Hutmacher, D. W.; Stevens, M. M.; Woodruff, M. A. Fabrication and in Vitro Characterization of Bioactive Glass Composite Scaffolds for Bone Regeneration. *Biofabrication* **2013**, *5* (4), 045005.
(32) Ren, J.; Blackwood, K. A.; Doustgani, A.; Poh, P. P.; Steck, R.; Stevens, M. M.; Woodruff, M. A. Melt-Electrospun Polycaprolactone Strontium-Substituted Bioactive Glass Scaffolds for Bone Regeneration. *J. Biomed Mater. Res. A* **2014**, *102* (9), 3140−3153.
(33) Nabiyouni, M.; Brueckner, T.; Zhou, H.; Gbureck, U.; Bhaduri, S. B. Magnesium-Based Bioceramics in Orthopedic Applications. *Acta Biomater* **2018**, *66*, 23−43.
(34) Wei, J.; Jia, J.; Wu, F.; Wei, S.; Zhou, H.; Zhang, H.; Shin, J. W.; Liu, C. Hierarchically Microporous/Macroporous Scaffold of Magnesium-Calcium Phosphate for Bone Tissue Regeneration. *Biomaterials* **2010**, *31* (6), 1260−1269.
(35) Gupta, M.; Wong, W. L. E. Magnesium-Based Nanocomposites: Lightweight Materials of the Future. *Mater. Charact* **2015**, *105*, 30−46.
(36) Zreiqat, H.; Howlett, C. R.; Zannettino, A.; Evans, P.; Schulze-Tanzil, G.; Knabe, C.; Shakibaei, M. Mechanisms of Magnesium-stimulated Adhesion of Osteoblastic Cells to Commonly Used Orthopaedic Implants. *Journal of Biomedical Materials Research: An Official Journal of The Society for Biomaterials, The Japanese Society for Biomaterials, and The Australian Society for Biomaterials and the Korean Society for Biomaterials* **2002**, *62* (2), 175−184.
(37) Eichholz, K. F.; von Euw, S.; Burdis, R.; Kelly, D. J.; Hoey, D. A. Development of a New Bone-Mimetic Surface Treatment Platform: Nanoneedle Hydroxyapatite (NnHA) Coating. *Adv. Healthc Mater.* **2020**, *9* (24), 2001102.
(38) Jenkins, T. L.; Little, D. Synthetic Scaffolds for Musculoskeletal Tissue Engineering: Cellular Responses to Fiber Parameters. *npj Regenerative Medicine 2019 4:1* **2019**, *4* (1), 1−14.
(39) Thibault, R. A.; Mikos, A. G.; Kasper, F. K. Scaffold/Extracellular Matrix Hybrid Constructs for Bone Tissue Engineering. *Adv. Healthc Mater.* **2013**, *2* (1), 13.
(40) Ali, S.; Khatri, Z.; Oh, K. W.; Kim, I. S.; Kim, S. H. Preparation and Characterization of Hybrid Polycaprolactone/Cellulose Ultrafine

Fibers via Electrospinning. *Macromolecular Research 2014 22:5* **2014**, *22* (5), 562−568.
(41) Calejo, I.; Costa-Almeida, R.; Reis, R. L.; Gomes, M. E. A Textile Platform Using Continuous Aligned and Textured Composite Microfibers to Engineer Tendon-to-Bone Interface Gradient Scaffolds. *Adv. Healthc Mater.* **2019**, *8* (15), 1900200.
(42) Jiang, W.; Li, L.; Zhang, D.; Huang, S.; Jing, Z.; Wu, Y.; Zhao, Z.; Zhao, L.; Zhou, S. Incorporation of Aligned PCL−PEG Nanofibers into Porous Chitosan Scaffolds Improved the Orientation of Collagen Fibers in Regenerated Periodontium. *Acta Biomater* **2015**, *25*, 240−252.
(43) Wang, W.; He, J.; Feng, B.; Zhang, Z.; Zhang, W.; Zhou, G.; Cao, Y.; Fu, W.; Liu, W. Aligned Nanofibers Direct Human Dermal Fibroblasts to Tenogenic Phenotype in Vitro and Enhance Tendon Regeneration in Vivo. *Nanomedicine* **2016**, *11* (9), 1055−1072.
(44) Staples, R.; Ivanovski, S.; Vaquette, C. Fibre-Guiding Biphasic Scaffold for Perpendicular Periodontal Ligament Attachment. *Acta Biomater* **2022**, *150*, 221−237.
(45) Komaki, M.; Iwasaki, K.; Arzate, H.; Narayanan, A. S.; Izumi, Y.; Morita, I. Cementum Protein 1 (CEMP1) Induces a Cementoblastic Phenotype and Reduces Osteoblastic Differentiation in Periodontal Ligament Cells. *J. Cell Physiol* **2012**, *227* (2), 649−657.
(46) Foster, B. L.; Ao, M.; Salmon, C. R.; Chavez, M. B.; Kolli, T. N.; Tran, A. B.; Chu, E. Y.; Kantovitz, K. R.; Yadav, M.; Narisawa, S.; Millán, J. L.; Nociti, F. H.; Somerman, M. J. Osteopontin Regulates Dentin and Alveolar Bone Development and Mineralization. *Bone* **2018**, *107*, 196−207.
(47) Du, J.; Li, M. Functions of Periostin in Dental Tissues and Its Role in Periodontal Tissues' Regeneration. *Cell. Mol. Life Sci.* **2017**, *74* (23), 4279−4286.

https://doi.org/10.1021/acsami.2c21256
ACS Appl. Mater. Interfaces 2023, 15, 12735−12749